Decomposing the Drivers of Polar Amplification with a Single Column Model

Matthew Henry*

College of Engineering, Mathematics and Physical Sciences, University of Exeter, Exeter, UK

Timothy M. Merlis

Department of Atmospheric and Oceanic Sciences, McGill University, Montreal, Quebec, Canada

Nicholas J. Lutsko

Scripps Institution of Oceanography, University of California at San Diego, La Jolla, CA, USA

Brian E.J. Rose

Department of Atmospheric and Environmental Sciences, University at Albany (State University of New York), USA

Corresponding author address: Matthew Henry, College of Engineering, Mathematics and Physical Sciences, Harrison Building, Streatham Campus, University of Exeter, North Park Road, Exeter, UK, EX4 4QF.

E-mail: m.henry@exeter.ac.uk

ABSTRACT

The precise mechanisms driving Arctic amplification are still under debate. Previous attribution methods based on top-of-atmosphere energy budgets have assumed all forcings and feedbacks lead to vertically-uniform temperature changes, with any departures from this collected into the lapse-rate feedback. We propose an alternative attribution method using a single column model that accounts for the forcing-dependence of high latitude lapse-rate changes. We test this method in an idealized General Circulation Model (GCM), finding that, even though the column-integrated carbon dioxide (CO_2) forcing and water vapor feedback are stronger in the tropics, they contribute to polar-amplified surface warming as they lead to bottom-heavy warming in high latitudes. A separation of atmospheric temperature changes into local and remote contributors shows that, in the absence of polar surface forcing (e.g., sea-ice retreat), changes in energy transport are primarily responsible for the polar amplified pattern of warming. The addition of surface forcing substantially increases polar surface warming and reduces the contribution of atmospheric dry static energy transport. This physically-based attribution method can be applied to comprehensive GCMs to provide a clearer view of the mechanisms behind Arctic amplification.

1. Introduction

The Arctic amplification of surface temperature change is a robust feature of observations (Stocker et al. 2013) and comprehensive climate model simulations (Pithan and Mauritsen 2014). A number of mechanisms are thought to contribute to Arctic amplification, including the surface albedo feedback, increased atmospheric energy transport convergence (Hwang and Frierson 2010), and the temperature feedback (Pithan and Mauritsen 2014); however, the precise contribution of each mechanism is still unclear. Clarifying how these different factors contribute to Arctic amplification is essential for reducing the uncertainty in the rate of Arctic warming through improved process-level understanding.

The tropics differ from the high latitudes in that they are close to radiative-convective equilibrium: heating by convection is balanced by radiative cooling, and the vertical temperature profile is mostly determined by surface temperature and humidity. The high latitudes, on the other hand, are close to radiative-advective equilibrium: warming from horizontal atmospheric heat transport is balanced by cooling from radiation. This means that different forcings and feedbacks induce different lapse rate responses. For example, an increase in longwave optical depth leads to bottom-heavy warming (Cronin and Jansen 2016; Henry and Merlis 2019), whereas atmospheric energy transport is thought to primarily affect the midtroposphere at high latitudes (Laliberté and Kushner 2013; Feldl et al. 2017a). This implies that the ratio between surface warming and top-of-atmosphere (TOA) net radiation changes at the high latitudes is different for each forcing and feedback. Surface temperature change attributions based on TOA budget analyses (Pithan and Mauritsen 2014) and moist energy balance models (Roe et al. 2015) assume a linear relationship between surface temperature change and TOA net radiation change that is independent of forcing. Hence these attribution methods neglect the dependence of the vertical structure of warming on

the perturbation type at high latitudes, and may produce misleading attributions of the drivers of Arctic amplification.

Process oriented and mechanism denial experiments are useful tools for studying the mechanisms responsible for Arctic amplification. For example, the analysis from Stuecker et al. (2018) suggests that local forcings and feedbacks dominate the polar-amplified pattern of surface temperature change in a comprehensive GCM in which CO_2 concentrations are increased in restricted latitudinal bands. Using the conventional TOA budget-based attribution method, they suggest that the lapse rate feedback is a main contributor to this surface temperature change pattern. Screen et al. (2012) attribute near-surface warming to local forcings and feedbacks and warming aloft to atmospheric energy transport increases by prescribing local and remote sea surface temperature (SST) and sea ice concentration (SIC) changes in two comprehensive atmospheric GCMs. However, fixing SST where the model would otherwise warm (or cool) the surface is akin to imposing a surface heat sink (or source), hence the results are not easily interpretable.

While these comprehensive GCM studies provide important insights into the mechanisms of Arctic amplification, a hierarchy of models is required for a complete understanding of the drivers of Arctic amplification in climate models and observations. Previous work using single column model representations of the high latitude atmosphere suggested that the high latitude temperature response is sensitive to the forcing type (Abbot and Tziperman 2008; Payne et al. 2015). Cronin and Jansen (2016) have developed a 1-dimensional model of an atmosphere in radiative-advective equilibrium for the high latitudes, which led to the important insight that high latitude lapse rate changes are forcing-dependent. The present work seeks to bridge the gap between their simple radiative-advective column model and complex climate model simulations in order to advance our understanding of the drivers of Arctic amplification.

Using an idealized moist atmospheric GCM with aquaplanet surface boundary conditions, no clouds, and no sea ice (hence no surface albedo feedback), we qualitatively reproduce the pattern of surface temperature change from comprehensive GCMs. To simulate the effect of melting sea ice, we impose a polar surface heat source, ranging from 0 to 24 $\mathrm{W\,m^{-2}}$. Then, we use a single column model (SCM) to emulate the tropics and high latitudes of the idealized GCM. This allows us to calculate the response to each individual forcing and feedback and thus decompose the drivers of tropical and polar temperature change. By accounting for each forcing and feedback's impact on the vertical structure of temperature change, this physically-based attribution method does not assume a universal high latitude lapse rate feedback, and, therefore, does not ignore how the vertical structure of temperature change depends on the perturbation. The idealized GCM acts as a test-case for the attribution method, which could potentially be used to untangle the contributions of the various mechanisms of polar amplification in comprehensive models or in observations.

2. Idealized atmospheric GCM

We use an idealized moist atmospheric GCM based on the Geophysical Fluid Dynamics Laboratory (GFDL) spectral dynamical core and the comprehensive radiation scheme of the GFDL AM2 GCM, with no sea ice or clouds. This is similar to the setup in Merlis et al. (2013) and to the Model of an Idealized Moist Atmosphere (MiMA, Jucker and Gerber (2017)). These GCMs follow the moist idealized GCM described in Frierson et al. (2006), but use comprehensive clear-sky radiation instead of grey radiation. In the MiMA setup, the surface albedo is globally uniform and increased to compensate for the cooling effect of clouds. In Merlis et al. (2013), an idealized cloud distribution is prescribed for the radiative transfer calculation. Here, there are no clouds and we set the surface albedo to a hemispherically symmetric analytic distribution similar to Earth's northern hemisphere TOA albedo, as estimated from the Cloud and the Earth's Radiant Energy

System data (Loeb et al. (2018), see supplemental figure S1), in order to produce an Earth-like meridional surface temperature gradient. The model uses the comprehensive radiation scheme described in Anderson et al. (2004) with annual mean solar insolation and a solar constant equal to 1365 $\mathrm{W\,m^{-2}}$.

The surface boundary condition is a slab mixed layer ocean aquaplanet with no representation of ocean heat transport and the heat capacity of 1m of water. We use annual-mean insolation and the small mixed layer depth allows the model to run quickly without meaningfully affecting the model's climate, as we only consider annual-mean quantities. The GCM was run at T42 spectral truncation, for a nominal horizontal resolution of 2.8° x 2.8°, and with 30 vertical levels. The skin temperature is interactively computed using the surface radiative and turbulent fluxes, which are determined by bulk aerodynamic formulae. A k-profile scheme with a dynamically determined boundary layer height is used to parameterize the boundary layer turbulence. The GCM uses a simplified Betts-Miller convection scheme (Frierson 2007), and large scale condensation is parameterized such that the relative humidity does not exceed one and condensed water is assumed to immediately return to the surface. As there is no representation of sea ice, there is no surface albedo feedback. To mimic the presence of the surface albedo feedback, we run perturbation experiments with an added polar surface heat source. All simulations are run for 20 years with time averages over the last 10 years shown, when all climate states have reached a statistical steady state.

We perform four simulations: a control run in which the atmospheric CO_2 concentration is set to 300 ppm, a run with quadrupled (1200 ppm) CO_2 concentration, and two runs with quadrupled CO_2 concentrations and constant surface heat sources Q_s of 12 $\mathrm{W\,m^{-2}}$ and 24 $\mathrm{W\,m^{-2}}$ poleward of 80° in both hemispheres. The heat sources simulate surface heating through the surface albedo feedback or increased oceanic energy transport convergence. Given that the polar surface tempera-

ture change under 4xCO_2 is approximately 8K, a 12 (24) $\mathrm{W\,m^{-2}}$ surface heat source is equivalent to a 1.5 (3) $\mathrm{W\,m^{-2}\,K^{-1}}$ local feedback. This can be compared to the locally defined surface albedo feedback from the models participating in the fifth coupled model intercomparison project (CMIP5) which is approximately 1 $\mathrm{W\,m^{-2}\,K^{-1}}$ in the Arctic and 2 $\mathrm{W\,m^{-2}\,K^{-1}}$ in the Antarctic (Feldl and Bordoni 2016, their figure 1).

Figure 1a shows the zonal-mean surface skin temperature differences between the control and three perturbation simulations, in addition to the zonal-mean surface temperature responses of abrupt 4xCO_2 experiments with 7 models participating in the sixth Coupled Model Intercomparison Project (CMIP6) listed in the legend of figure 1 (Eyring et al. 2016). Figure 1b shows the surface temperature changes normalized by their global mean. The patterns of surface temperature change from the idealized model experiments (black) approximately span the CMIP6 model responses (colors). The amount of Arctic amplification is underestimated in the 4xCO_2 experiment, but adding a polar surface heat source brings the idealized GCM closer to CMIP6 in the Arctic, with high latitude warming of 2 to 3 times the global-mean surface temperature change. Note that the CMIP6 temperature changes are not fully equilibrated, and, at equilibrium, the Antarctic is also expected to have amplified warming, but this warming is transiently delayed by ocean heat uptake (Manabe et al. 1991; Rugenstein et al. 2019).

3. Single column model

To emulate the tropical and high-latitude atmosphere of the idealized GCM, we use the single column model (SCM) from the ClimLab python package for process-oriented climate modeling Rose (2018). The temperature tendency budgets for atmospheric and surface temperature are given by the following equations:

$$\frac{\partial T_{atm}(p)}{\partial t} = \left.\frac{\partial T_{atm}(p)}{\partial t}\right|_{rad} + \left.\frac{\partial T_{atm}(p)}{\partial t}\right|_{conv} + \left.\frac{\partial T_{atm}(p)}{\partial t}\right|_{adv} + \left.\frac{\partial T_{atm}(p)}{\partial t}\right|_{cond} \quad (1)$$

$$\frac{\partial T_s}{\partial t} = \left.\frac{\partial T_s}{\partial t}\right|_{rad} + \left.\frac{\partial T_s}{\partial t}\right|_{SH} + \left.\frac{\partial T_s}{\partial t}\right|_{LH}, \quad (2)$$

where t is time and p is pressure (with 40 pressure levels). The subscripts 'rad', 'conv', 'adv', and 'cond', 'SH', 'LH' refer to radiative, convective, advective, condensation, sensible heat flux, and latent heat flux temperature tendencies, respectively. The radiative, convective, sensible heat flux, and latent heat flux temperature tendencies are computed interactively. The RRTMG radiation scheme is used for the computation of shortwave and longwave radiative temperature tendencies. The surface albedo and control insolation are set such that the upwelling and downwelling TOA shortwave radiation match the idealized GCM simulations in the tropics (10°S to 10°N) and poleward of 80°. Convection is implemented as an adjustment of the temperature profile to the moist adiabat, whereas the idealized GCM uses a simplified Betts-Miller convection scheme (Frierson 2007). Note that at high latitudes, horizontal atmospheric energy transport induces a temperature structure stable to convection, hence convection has no effect. The surface sensible and latent heat fluxes are computed using bulk aerodynamic formulae with 5×10^{-2} drag coefficient and 5 ms^{-1} near surface wind speed (Rose 2018).

Values from the idealized GCM experiments averaged in the tropics (10°S to 10°N) and poleward of 80°N are used to prescribe the specific humidity profile, which affects the radiation and surface latent heat flux. In addition, the time-mean advection and condensation temperature tendency profiles from the idealized GCM simulations are added as external temperature tendency terms to simulate the dry and moist components of atmospheric energy transport convergence, respectively (see supplementary figure S2 for the temperature tendency profiles). The advective

temperature tendency term is calculated in the GCM as the difference in temperature tendency before and after running the dynamics module, hence it contains the horizontal and vertical advection temperature tendencies.

The climatological temperature profiles of the idealized GCM and SCM are similar (figure 2), though the SCM has an overly strong near-surface temperature inversion compared to the GCM. This may be due to the absence of boundary layer scheme in the SCM, which would smooth differences between the surface and lower atmospheric layers. Similarities between the temperature profiles simulated by the idealized GCM and by the SCM still hold when the latitudinal bounds of the tropics are set to 20°S-20°N and the high latitudes to 60° (see supplementary figure S3).

4. Attribution of idealized GCM tropical and polar lapse rate changes to forcings and feedbacks.

As discussed in the introduction, the forcing dependence of the high latitude lapse rate feedback makes a TOA budget approach to attributing the polar surface warming to different forcings and feedbacks ambiguous (see next section). The SCM allows us to attribute the idealized GCM's tropical and polar lapse rate changes to the different forcings and feedbacks. We individually perturb CO_2, water vapor, and atmospheric energy transport (moist and dry components) in the tropics and high latitudes to attribute the total warming to each of these individual components.

Figure 3 shows the decomposition of (a) tropical and (b,c,d) polar lapse rate changes of the three idealized GCM perturbation experiments: 4xCO_2 (a,b), 4xCO_2 with Q_s=12 $\mathrm{W\,m^{-2}}$ (a,c) and Q_s=24 $\mathrm{W\,m^{-2}}$ (a,d); Table 1 summarizes the surface temperature change attributions.

The tropical lapse rate changes for the three experiments are similar enough to be plotted in the same figure 3a: the $Q_s = 12\mathrm{W\,m^{-2}}$ and $Q_s = 24\mathrm{W\,m^{-2}}$ experiment changes are shown in dashed and dash-dotted respectively, and fall close to each other. They are decomposed into the tempera-

ture change from the CO_2 forcing (red), water vapor feedback (blue), and energy transport (green). For each GCM experiment, the SCM's response to applying all of the perturbations simultaneously (black) is exactly the same as the sum of the responses to the individual perturbations and fits the idealized GCM's response well throughout the troposphere (grey), demonstrating the accuracy of the attribution method. Differences in the stratosphere between the SCM and idealized GCM may be due to the different radiation schemes or ozone distributions. Since convection is triggered in the tropics, the temperature profiles are moist adiabatic and the vertical structure of tropospheric temperature change ($\Delta T/\Delta T_S$) is approximately the same for all SCM experiments. The energy transport is slightly reduced in the experiments with surface heat sources.

The polar lapse rate changes (b,c,d) are decomposed into the temperature changes from the CO_2 forcing (red), water vapor feedback (blue), the 'local' water vapor feedback (blue dashed, see section 6), the energy transport (dry component in orange and moist component in cyan), and surface heat source (yellow). Again, for each GCM experiment, the SCM's response to applying all of the perturbations simultaneously (black) is exactly the same as the sum of the responses to the individual perturbations, and fits the idealized GCM's response well throughout the troposphere (grey), showing the accuracy of the attribution method. The increase in longwave absorbers (CO_2 and water vapor) leads to bottom-heavy warming, the dry component of energy transport leads to top-heavy warming, the moist component of energy transport leads to mid-troposphere enhanced warming, and the surface heat source leads to very bottom-heavy warming.

The polar surface temperature change is 3.6K and 7.6K higher in the $Q_s = 12\mathrm{W\,m^{-2}}$ and $Q_s = 24\mathrm{W\,m^{-2}}$ cases respectively, which is caused mainly by 4.6K and 8.9K warming, respectively, due to the surface heat source. The reduction in the dry component of energy transport causes a 2.1K and 4.1K cooling respectively versus no warming in the simulation with $Q_s = 0\mathrm{W\,m^{-2}}$. There are also slight increases in warming due to the water vapor feedback (discussed in section

6) and moist component of the energy transport compared to the 4xCO_2 experiment (Table 1). This is consistent with Hwang et al. (2011), who found that enhanced Arctic warming due to local feedbacks weakens the equator-to-pole temperature gradient and reduces the dry component of the atmospheric energy transport, which outweighs the increase in the moist component of atmospheric energy transport that arises from the enhanced warming.

5. Surface temperature change attribution method comparison

The conventional surface temperature change attribution method (Pithan and Mauritsen 2014; Stuecker et al. 2018) assumes forcings and feedbacks lead to vertically uniform temperature changes. The deviation from vertically uniform temperature change is then accounted for in the lapse rate feedback. One can decompose the surface temperature change as follows (equation 3 in the Methods section of Stuecker et al. (2018)):

$$\Delta T_S(\phi) = (-\frac{1}{\overline{\lambda_P}})\{\Delta T_S(\phi)[\lambda'_P(\phi) + \lambda_{LR}(\phi) + \lambda_{WV}(\phi) + \lambda_{AL}(\phi)] + \mathscr{F}(\phi) + \Delta(\nabla \cdot \vec{F}(\phi))\} \quad (3)$$

where ϕ is the latitude. The surface temperature change attributions are then given by the average of $\Delta T_S(\phi)$ over the tropics and Arctic. The Planck feedback is decomposed into its global-mean $\overline{\lambda_P}$ and its deviation λ'_P, λ_{LR} is the lapse rate feedback, λ_{WV} is the water vapor feedback, λ_{AL} is the surface albedo feedback and λ_{CL} is the cloud feedback.

To apply the conventional attribution method to the GCM simulations, we use aquaplanet kernels from Feldl et al. (2017b) (available at https://github.com/nfeldl/aquakernels) to calculate the feedbacks. The CO_2 forcing $\mathscr{F}$ is computed as the change in TOA net radiation between the control simulation and an idealized GCM simulation where sea surface temperatures (SST) are fixed to the control SST and CO_2 concentrations are quadrupled (Hansen et al. 2005). The change in

atmospheric energy transport convergence $\Delta(\nabla \cdot \vec{F})$ is computed as the change in net TOA radiation (minus the surface forcing) between the control and perturbed simulations. This method of attributing surface temperature changes to forcings and feedbacks then tells us how much surface temperature change is required to balance the TOA energy imbalance caused by each forcing or feedback, assuming the atmospheric temperature change is vertically uniform (except for the lapse rate feedback).

Figure 4 compares this TOA energy budget surface temperature change attribution method (crosses) with the single column model based attribution method (filled circles) for the 4xCO_2 (a), 4xCO_2 with $Q_s = 12\mathrm{W\,m^{-2}}$ (b) and $Q_s = 24\mathrm{W\,m^{-2}}$ (c). The tropical (x-axis, 10°S to 10°N) and polar (y-axis, 80°N to 90°N) attributions are plotted against each other. If a point falls above (below) the one-to-one line, the forcing or feedback contributes to polar (tropical) amplification. As in Pithan and Mauritsen (2014), the TOA attribution method suggests that the Planck and lapse rate feedbacks contribute to polar amplification. The lapse rate feedback contributes to more polar amplification in the surface heat source experiments. The single column model attribution method, in contrast, has no temperature feedback in its decomposition. Since the TOA energy budget method assumes that the temperature response to a TOA energy imbalance is vertically uniform, it will attribute a larger (smaller) amplitude change in surface temperature than the single column model if the response to the forcing or feedback is top-heavy (bottom-heavy). In the tropics, all temperature changes are top-heavy as they follow the moist adiabat, hence the SCM attributions are all closer to the y-axis than the corresponding TOA method attributions. In the high latitudes, the SCM temperature changes from increases in CO_2, water vapor, and surface heat source are bottom-heavy, hence they all contribute a larger surface temperature change than is diagnosed from the TOA method. The energy transport convergence change leads to top-heavy

warming, hence the warming attributed to it by the SCM method is smaller than the warming attributed by the TOA method, and even negative in the surface heat source cases.

In summary, we underline two main points from this comparison of the single column model and TOA-based surface temperature change attribution methods:

- The increase in longwave absorbers (CO_2 and water vapor) go from contributing to tropical amplification in the TOA attribution method to contributing to polar amplification in the SCM attribution method. The forcing from CO_2 and the water vapor feedback are stronger in the tropics than the high latitudes, but since the tropical SCM attribution includes the effect of convection, the warming maximum is pushed to the upper-troposphere and there is less surface warming. In the high latitudes however, an increase in longwave absorbers leads to bottom-heavy warming (Cronin and Jansen 2016; Henry and Merlis 2019). Russotto and Biasutti (2020) analyze the response of atmospheric GCMs using a moist energy balance model, and similarly find that a tropically amplified CO_2 forcing and water vapor feedback lead to a polar amplified temperature response.

- Since the increase in atmospheric energy transport convergence preferentially affects the mid-troposphere, it leads to less surface warming at high latitudes, and even surface cooling in the surface heat source experiments.

6. Local and remote drivers of temperature change.

The SCM attribution method can also be used to decompose the drivers of polar amplification into local and remote drivers. The CO_2 and surface heat source perturbations are local drivers, while the energy transport can be considered as a remote driver. The water vapor feedback includes both local and remote contributions. First, the change in specific humidity can be decomposed

into a temperature-dependent change and a change due to relative humidity: $\Delta q = \Delta q|_{fixedRH} + \Delta RH \times q^*|_{clim}$ where $q^*|_{clim}$ is the climatological saturation specific humidity. Since the relative humidity in the idealized GCM stays relatively constant (supplementary figure S4), we ignore the second term of this equation. Using fixed relative humidity (RH) SCM experiments, we can decompose the temperature-dependent changes in specific humidity into the 'local' changes in response to the temperature changes forced by increased CO_2 and the surface heat source, and the 'remote' changes in response to the temperature change forced by altered energy transports: $\Delta q \approx \Delta q|_{fixedRH} = \Delta q|_{fixedRH,\Delta CO_2,\Delta Q_s} + \Delta q|_{fixedRH,\Delta ET}$.

This local versus remote decomposition of the water vapor concentration increase is not perfect, as it assumes the energy transport simply affects the humidity of the high latitudes by changing its temperature and activating the local water vapor feedback, whereas the general circulation can directly advect water vapor. The energy transport term also contains vertical advection, which can change as a result of local diabatic forcings (shown in magenta in supplementary figure S2). Moreover, GCM experiments where the forcing from a CO_2 increase is constrained to the high latitudes show changes in energy transport, which would also affect the water vapor feedback (Stuecker et al. 2018). Since energy transport is affected by both temperature and humidity gradients, it is not clear that any perfect local / remote decomposition exists. Nevertheless, our definition of 'local' recovers traditional SCM treatments of fixed relative humidity water vapor feedback (Manabe and Wetherald 1967) in the limit of no energy transport change.

The fixed-RH SCM simulations have the same modules and parameters as the standard SCM simulations, but instead of prescribing the idealized GCM's specific humidity, they have fixed relative humidity and the specific humidity is free to evolve with the temperature. The climatological temperature of the fixed RH SCMs have a warm bias (supplementary figure S5) and the climatological specific humidity is biased high (supplementary figures S6). We do two sets of fixed-RH

SCM experiments: the first ('local') experiment is forced with the increase in CO_2 concentration (and surface heat source), and the second is forced with increased CO_2 concentration (and surface heat source) and perturbed energy transport. The latter has less tropical warming and similar polar warming compared to the idealized GCM (red lines in supplementary figure S7 for the 4xCO_2 experiment), and similar changes in specific humidity in the tropics and a higher increase in high latitudes compared to the idealized GCM (red lines in supplementary figures S8 for the 4xCO_2 experiment). The 'local' increase in water vapor, $\Delta q|_{fixedRH,\Delta CO_2,\Delta Q_s}$, is taken to be the change in water vapor from the first set of fixed-RH SCM experiments (blue lines in figure S8 for the 4xCO_2 experiment), and the 'remote' increase in water vapor, $\Delta q|_{fixedRH,\Delta ET}$, is taken to be the residual between the total change in water vapor and the 'local' change in water vapor. We then force the original SCM with the 'local' and 'remote' specific humidity changes to deduce the 'q (local)' and 'q (remote)' temperature changes (shown in table 2). The 'q (local)' experiments are comparable to the fixed RH experiments in Payne et al. (2015). The temperature changes from the high latitude 'q (local)' experiments are shown in figure 3 (blue dashed).

Table 2 summarizes the result of this local / remote decomposition of surface temperature change. In the three perturbation experiments, the warming from CO_2 alone is 1.8K in the tropics and 3.1K at high latitudes, hence increasing CO_2 leads to polar amplification in the absence of any feedbacks. The addition of the 'local' water vapor feedback increases the tropical surface warming to 7.5K and the polar surface warming to 4.0K in the 4xCO_2 experiment, and thus cancels the polar amplification from CO_2 alone. Payne et al. (2015) also found a tropical amplification of surface temperature change in their fixed-RH SCM simulations, though with somewhat different magnitude. Finally, adding the atmospheric energy transport and its implied water vapor change decreases the tropical surface warming to 3.7K, and increases the polar surface warming to 9.0K in the 4xCO_2 experiment, thus leading to polar amplification. The polar surface heat source gen-

erally increases the amount of polar amplification despite the partial compensation by a reduction in dry energy transport. For the 4xCO_2 experiment, approximately half of the polar warming is due to local sources (4.0K out of 9K of total warming), but the polar amplified pattern of warming is primarily caused by the increase in atmospheric energy transport which cools the tropics and warms the high latitudes. The high latitude warming is then strongly enhanced by the increased water vapor from remote sources. When a polar surface heat source is added, almost all of the polar surface warming is due to local sources because of the surface heat source and the compensating reduction in the dry component of energy transport: 10.2K and 16.1K from local sources for a total warming of 12.6K and 16.6K for the $Q_s = 12\mathrm{W\,m^{-2}}$ and $Q_s = 24\mathrm{W\,m^{-2}}$ experiments, respectively.

7. Summary and discussion

Unlike the tropics which are close to radiative-convective equilibrium, the high latitudes are in radiative-advective equilibrium: different forcings and feedbacks induce different lapse rate responses. Previous surface temperature attributions have assumed that different forcings and feedbacks induce vertically homogeneous warming, and attributed the deviation from vertically uniform warming to the lapse rate feedback. In these attributions, the lapse rate feedback functions as a residual that cannot be clearly ascribed to any particular physical process.

We introduce a surface temperature change attribution method based on a single column model, which accounts for the vertically inhomogeneous temperature change contributions of each forcing and feedback. We find that the warming from increased longwave absorbers (CO_2 and water vapor) is bottom-heavy and accounts for most of the surface warming in the absence of a surface heat source. By contrast, the warming from atmospheric heat transport preferentially warms the mid and upper troposphere. When a polar surface heat source is added, there is a reduction in the

dry component of atmospheric energy transport which partially compensates for the extra surface warming from the polar surface heat source. Compared to the conventional surface temperature change attribution method, the increase in longwave absorbers (CO_2 and water vapor) goes from contributing to tropical amplification to polar amplification. In addition, the polar warming contribution from the increase in atmospheric energy transport convergence is reduced as it preferentially warms the mid and upper troposphere. Finally, we separated the drivers of atmospheric temperature change into local and remote contributors and found that, in the absence of a polar surface heat source, the change in energy transport was primarily responsible for the polar amplified pattern of warming. The addition of a polar surface heat source increases the contribution of local drivers to polar warming at the expense of remote drivers, as the dry energy transport is reduced.

It is important to note that clouds and sea ice were ignored in this analysis (aside from the surface heat source that mimics the effects of shortwave cloud feedbacks and sea ice), though they may play an important role in explaining the pattern of surface temperature change in comprehensive climate model simulations. Arctic amplification also has seasonality — it is strong in winter and suppressed in summer — which has been suggested to result from the increased polar ocean heat uptake in summer and ocean heat release in winter from the melting sea ice (Manabe and Stouffer 1980; Bintanja and Van der Linden 2013; Dai et al. 2019). Nevertheless, we believe that the single-column model can be a stepping stone for connecting simple physical models with comprehensive climate models: clouds and seasonality can be prescribed in the SCM, which would be a valuable extension of the present work. This would allow us to understand the basic mechanisms driving Arctic amplification and reduce the uncertainty in the rate of Arctic warming.

Acknowledgments. The code and data needed to reproduce all figures, tables and supplementary figures will be made available at https://github.com/matthewjhenry/HMLR19_SCM. Documentation for the python ClimLab package can be found at https://climlab.readthedocs.io/. The top-of-atmosphere albedo data from the Cloud and the Earth's Radiant Energy System (CERES) can be found at https://ceres.larc.nasa.gov/. The CMIP6 data is available on the Earth System Grid Federation database. This work was supported by a Natural Sciences and Research Council (NSERC) Discovery grant and Canada Research Chair, as well as a Compute Canada allocation. B.E.J.R was supported by NSF grant AGS-1455071.

References

Abbot, D. S., and E. Tziperman, 2008: Sea ice, high-latitude convection, and equable climates. *Geophysical Research Letters*, **35 (3)**.

Anderson, J. L., and Coauthors, 2004: The new GFDL global atmosphere and land model AM2–LM2: Evaluation with prescribed SST simulations. *Journal of Climate*, **17 (24)**, 4641–4673.

Bintanja, R., and E. Van der Linden, 2013: The changing seasonal climate in the arctic. *Scientific Reports*, **3**, 1556.

Cronin, T. W., and M. F. Jansen, 2016: Analytic radiative-advective equilibrium as a model for high-latitude climate. *Geophysical Research Letters*, **43 (1)**, 449–457.

Dai, A., D. Luo, M. Song, and J. Liu, 2019: Arctic amplification is caused by sea-ice loss under increasing co 2. *Nature communications*, **10 (1)**, 121.

Eyring, V., S. Bony, G. A. Meehl, C. A. Senior, B. Stevens, R. J. Stouffer, and K. E. Taylor, 2016: Overview of the coupled model intercomparison project phase 6 (CMIP6) experimental design and organization. *Geoscientific Model Development (Online)*, **9 (LLNL-JRNL-736881)**.

Feldl, N., B. T. Anderson, and S. Bordoni, 2017a: Atmospheric eddies mediate lapse rate feedback and arctic amplification. *Journal of Climate*, **30 (22)**, 9213–9224.

Feldl, N., and S. Bordoni, 2016: Characterizing the Hadley circulation response through regional climate feedbacks. *J. Climate*, **29 (2)**, 613–622.

Feldl, N., S. Bordoni, and T. M. Merlis, 2017b: Coupled high-latitude climate feedbacks and their impact on atmospheric heat transport. *Journal of Climate*, **30 (1)**, 189–201.

Frierson, D. M., 2007: The dynamics of idealized convection schemes and their effect on the zonally averaged tropical circulation. *J. Atmos. Sci.*, **64 (6)**, 1959–1976.

Frierson, D. M., I. M. Held, and P. Zurita-Gotor, 2006: A gray-radiation aquaplanet moist GCM. part I: Static stability and eddy scale. *Journal of the Atmospheric Sciences*, **63 (10)**, 2548–2566.

Hansen, J., and Coauthors, 2005: Efficacy of climate forcings. *J. Geophys. Res.*, **110**, D18 104.

Henry, M., and T. M. Merlis, 2019: Forcing dependence of atmospheric lapse rate changes dominates residual polar warming in solar radiation management scenarios. *(In review)*.

Hwang, Y.-T., and D. M. Frierson, 2010: Increasing atmospheric poleward energy transport with global warming. *Geophysical Research Letters*, **37 (24)**.

Hwang, Y.-T., D. M. Frierson, and J. E. Kay, 2011: Coupling between Arctic feedbacks and changes in poleward energy transport. *Geophysical Research Letters*, **38 (17)**.

Jucker, M., and E. Gerber, 2017: Untangling the annual cycle of the tropical tropopause layer with an idealized moist model. *Journal of Climate*, **30 (18)**, 7339–7358.

Laliberté, F., and P. Kushner, 2013: Isentropic constraints by midlatitude surface warming on the arctic midtroposphere. *Geophysical Research Letters*, **40 (3)**, 606–611.

Loeb, N. G., and Coauthors, 2018: Clouds and the earth's radiant energy system (CERES) energy balanced and filled (EBAF) top-of-atmosphere (TOA) edition-4.0 data product. *Journal of Climate*, **31 (2)**, 895–918.

Manabe, S., R. Stouffer, M. Spelman, and K. Bryan, 1991: Transient responses of a coupled ocean–atmosphere model to gradual changes of atmospheric CO_2. Part 1. annual mean response. *J. Climate*, **4 (8)**, 785–818.

Manabe, S., and R. J. Stouffer, 1980: Sensitivity of a global climate model to an increase of CO2 concentration in the atmosphere. *Journal of Geophysical Research: Oceans*, **85 (C10)**, 5529–5554.

Manabe, S., and R. T. Wetherald, 1967: Thermal equilibrium of the atmosphere with a given distribution of relative humidity. *Journal of the Atmospheric Sciences*, **24 (3)**, 241–259.

Merlis, T. M., T. Schneider, S. Bordoni, and I. Eisenman, 2013: Hadley circulation response to orbital precession. part I: Aquaplanets. *Journal of Climate*, **26 (3)**, 740–753.

Payne, A. E., M. F. Jansen, and T. W. Cronin, 2015: Conceptual model analysis of the influence of temperature feedbacks on polar amplification. *Geophys. Res. Lett.*, 9561–9570.

Pithan, F., and T. Mauritsen, 2014: Arctic amplification dominated by temperature feedbacks in contemporary climate models. *Nat. Geosci.*, **7**, 181–184.

Roe, G. H., N. Feldl, K. C. Armour, Y.-T. Hwang, and D. M. Frierson, 2015: The remote impacts of climate feedbacks on regional climate predictability. *Nature Geoscience*, **8 (2)**, 135.

Rose, B. E., 2018: Climlab: A python toolkit for interactive, process oriented climate modeling. *J. Open Source Software*, **3 (24)**, 659.

Rugenstein, M., and Coauthors, 2019: LongRunMIP–motivation and design for a large collection of millennial-length AO-GCM simulations. *Bulletin of the American Meteorological Society*, **(2019)**.

Russotto, R. D., and M. Biasutti, 2020: Polar amplification as an inherent response of a circulating atmosphere: results from the TRACMIP aquaplanets. *Geophysical Research Letters*, **(In Review)**.

Screen, J. A., C. Deser, and I. Simmonds, 2012: Local and remote controls on observed arctic warming. *Geophysical Research Letters*, **39 (10)**.

Stocker, T. F., and Coauthors, Eds., 2013: *Climate Change 2013: The Physical Science Basis*. Cambridge University Press, Cambridge and New York.

Stuecker, M. F., and Coauthors, 2018: Polar amplification dominated by local forcing and feedbacks. *Nature Climate Change*, **8 (12)**, 1076.

LIST OF TABLES

Forcing ($W\,m^{-2}$) / Feedback ($W\,m^{-2}\,K^{-1}$)	$4xCO_2$	$4xCO_2$ + 12 $W\,m^{-2}$	$4xCO_2$ + 24 $W\,m^{-2}$
Tropics			
CO_2	1.8	1.8	1.8
Water Vapor	2.8	2.9	2.9
ET	-0.8	-0.5	-0.5
Tropics total	**3.7**	**4.0**	**4.1**
Pole			
CO_2	3.1	3.1	3.1
Water Vapor	4.3	4.8	5.5
ET (dry)	0	-2.1	-4.1
ET (moist)	1.4	2.0	2.8
Q_s	0	4.6	8.9
Pole total	**9.0**	**12.6**	**16.6**

TABLE 1. Surface temperature change attribution based on the single column model decomposition for the three perturbation experiments. 'CO_2' and 'Water Vapor' denote the radiative effect of their increase on surface temperature, whereas 'ET' denotes the effect of the change in energy transport on surface temperature and is decomposed into its dry and moist components in the pole. 'Q_s' denotes the effect of the surface heat source on the surface temperature change.

Forcing / feedback	Tropics	Pole ($4xCO_2$)	Pole ($4xCO_2$+12)	Pole ($4xCO_2$+24)
CO_2	1.8	3.1	3.1	3.1
q (local)	5.7	0.9	2.5	4.1
Q_s	0	0	4.6	8.9
Local total	**7.5**	**4.0**	**10.2**	**16.1**
q (remote)	-2.9,-2.8,-2.8	3.4	2.3	1.4
ET	-0.8,-0.5,-0.5	1.5	-0.1	-1.4
Remote total	**-3.8,-3.4,-3.4**	**4.9**	**2.2**	**0**
Total	**3.7,4.0,4.1**	**9.0**	**12.6**	**16.6**

TABLE 2. Surface temperature change attribution based on the single column model decomposition for the three perturbation experiments. The tropical surface temperature change attributions are sufficiently similar to be in a single column. The three successive values separated by a comma refer to the the $4xCO_2$, $Q_s = 12\mathrm{W\,m^{-2}}$, and $Q_s = 24\mathrm{W\,m^{-2}}$ experiments respectively. Slight discrepancies between the total and the sum of local and remote totals occur as the total is the surface temperature change from the experiment with all perturbations.

LIST OF FIGURES

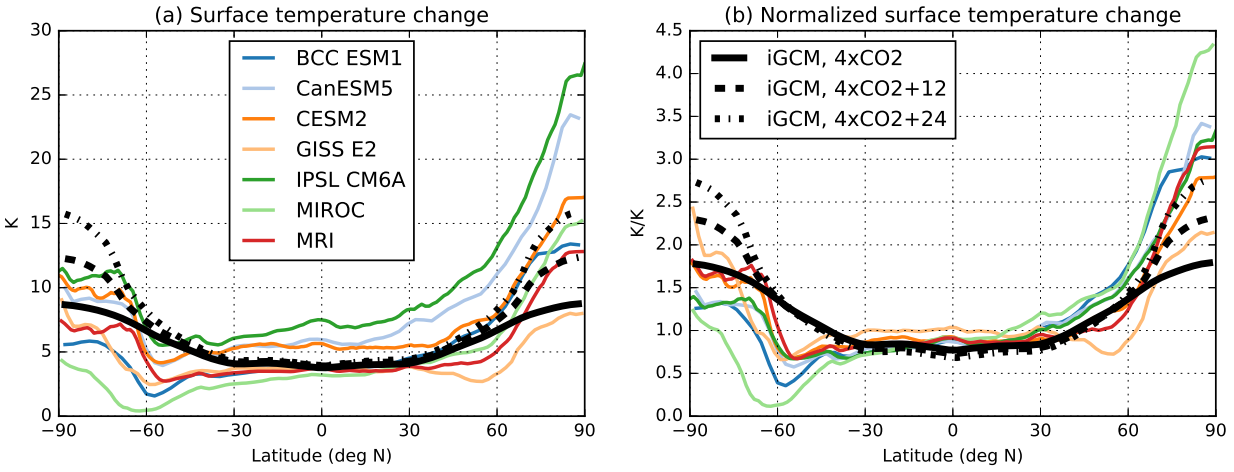

535 FIG. 1. (a) Surface temperature difference between the control experiment (300ppm CO_2 concentration)
536 and increased CO_2 experiment (1200ppm) (black) and increased CO_2 experiment (1200ppm) with a 12 $W\,m^{-2}$
537 (black dashed) and 24 $W\,m^{-2}$ (black dash-dot) surface heat source poleward of 80° using an idealized moist
538 atmospheric GCM with no clouds or sea ice. These are compared to CMIP6 abrupt 4xCO_2 surface temperature
539 changes in simulations with the following models: BCC-ESM1, CanESM5, CESM2, GISS-E2, IPSL CM6A,
540 MIROC, MRI. (b) Same as (a), but the temperature changes are normalized by global mean surface temperature
541 change.

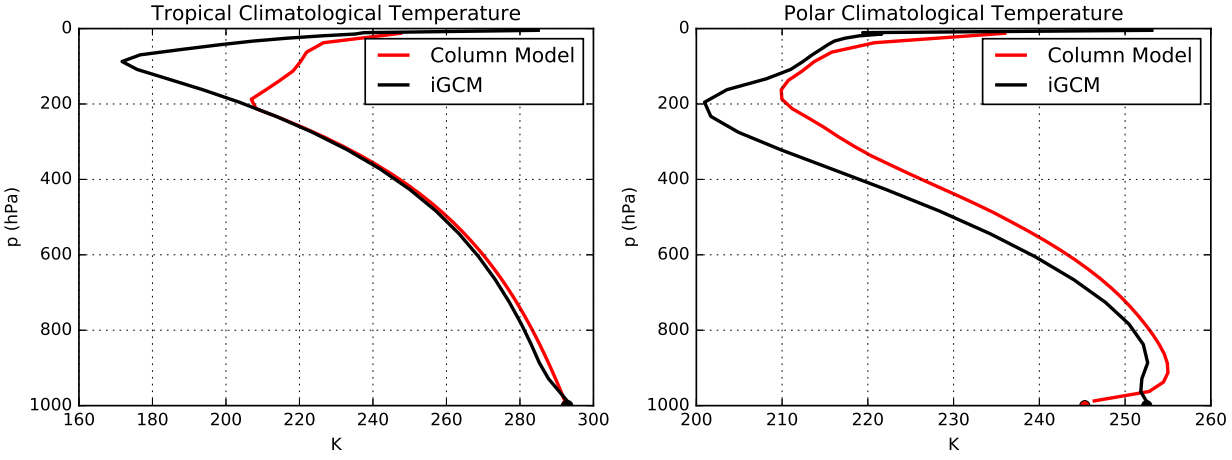

542 FIG. 2. Comparison between the single column model (red) and idealized GCM (black) for the (a) tropical
543 ($|\text{lat}|<10°$) climatological temperature and (b) the polar (lat$>80°$ North) climatological temperature.

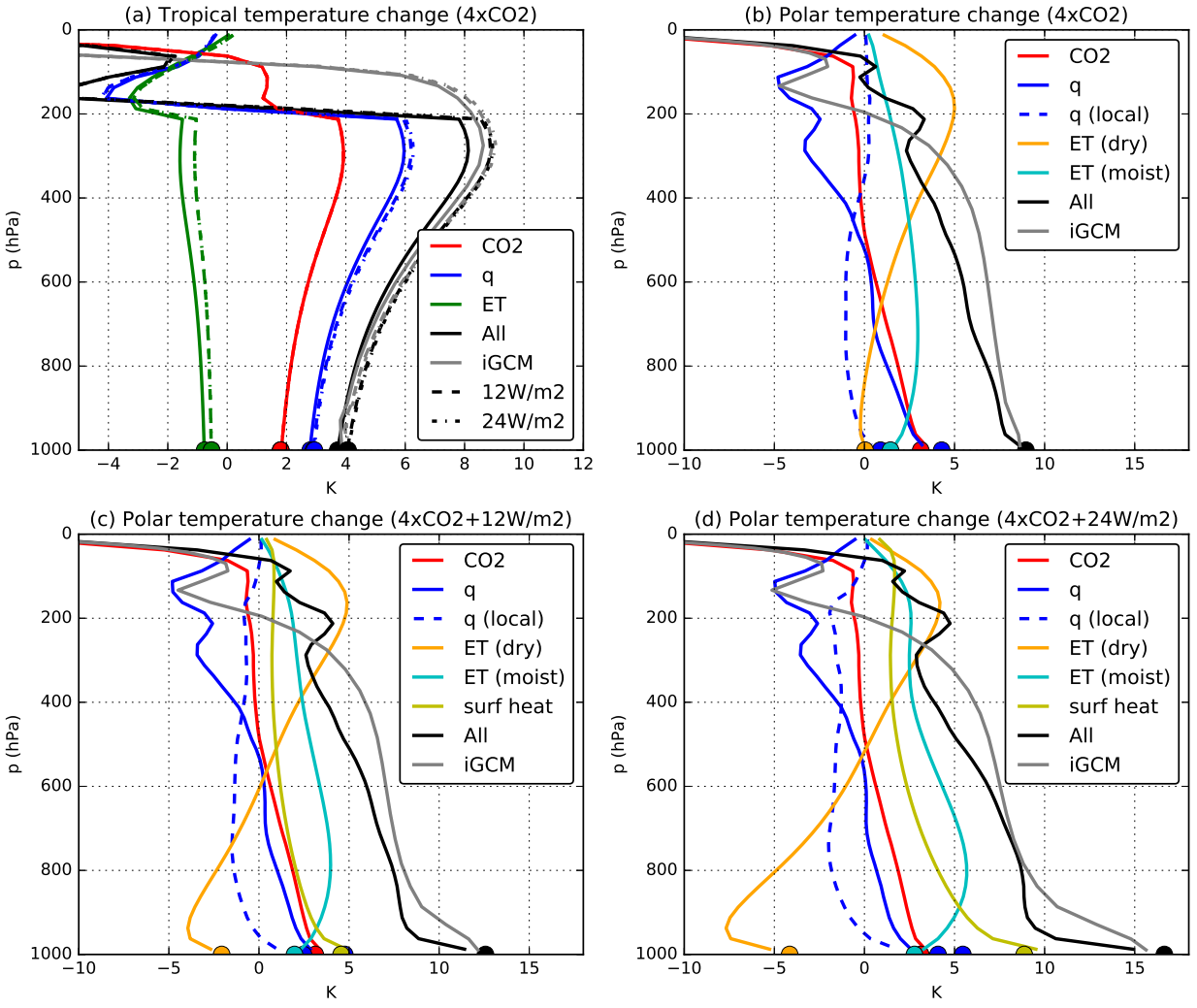

FIG. 3. Tropical (a) and polar (b,c,d) temperature change for the idealized GCM (grey) and three perturbation experiments using the single column model: 4xCO_2 (a,b), 4xCO_2 with 12 W m^{-2} surface heat source poleward of 80° (a,c), and 4xCO_2 with 24 W m^{-2} surface heat source poleward of 80° (a,d). The SCM experiments with all changes (black) are exactly the same as the sum of individual changes and fit the idealized GCM (grey) well. The individual forcing and feedback contributions are calculated by individually perturbing them in the single column model (colors). They include the CO_2 increase (red), the water vapor feedback (blue), the 'local' water vapor feedback (blue dashed, see section 6), the energy transport (green in tropics, separated into dry (orange) and moist (cyan) in high latitudes), and the surface heat source (yellow). The tropical temperature changes of the three experiments (a) are similar enough to be plotted together (12 W m^{-2} in dashed lines and 24 W m^{-2} in dash-dotted lines). Surface temperature change attributions are summarized in table 1.

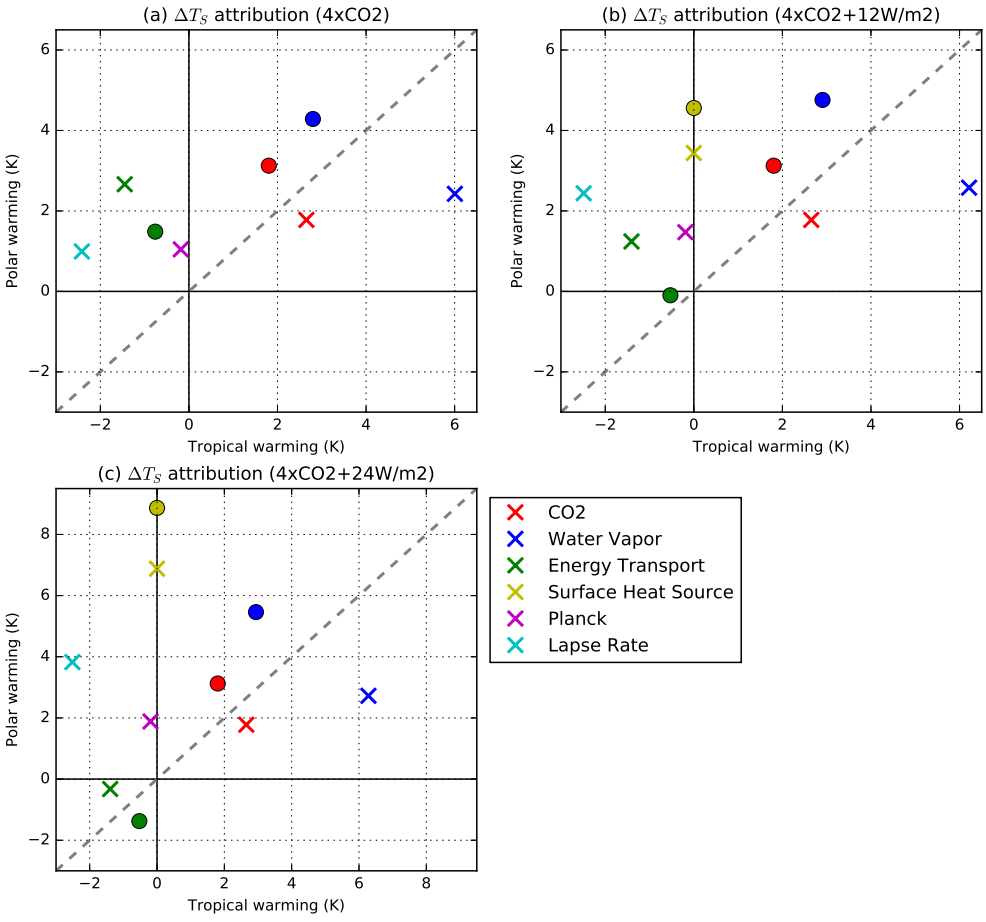

554 FIG. 4. Surface temperature change attributions for the 4xCO_2 (a) and 4xCO_2 with $Q_s = 12\,\mathrm{W\,m^{-2}}$ (b) and
555 $Q_s = 24\,\mathrm{W\,m^{-2}}$ (c) using the TOA energy budget method (crosses) and the SCM method presented in this paper
556 (dots). Presented are the surface temperature change attributions to the increase in CO_2 (red), water vapor (blue),
557 energy transport (green), surface heat source (yellow) for both methods. The Planck (magenta) and lapse rate
558 (cyan) feedback contributions are also shown for the TOA energy budget method. When the point is above
559 (below) the one-to-one line, the forcing or feedback contributes to polar (tropical) amplification.

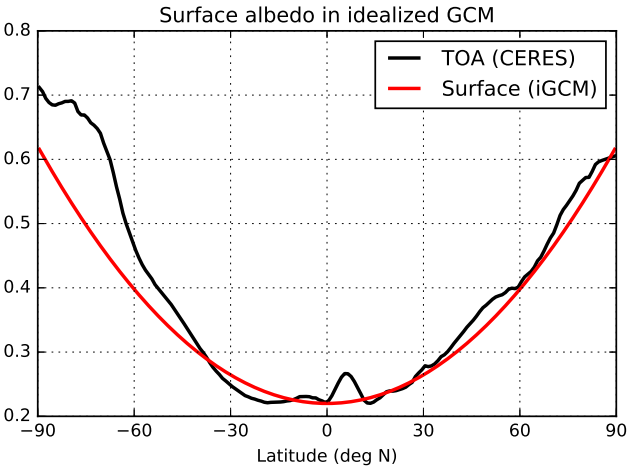

560 Fig. S1. Surface albedo used in idealized GCM calculated using following formula: $0.22 + 0.4 * (lat/90)^2$
561 (red). Annual-mean zonally averaged climatology (07/2005 - 06/2015) of top-of-atmosphere albedo with data
562 from Cloud and the Earth's Radiant Energy System (CERES) (black).

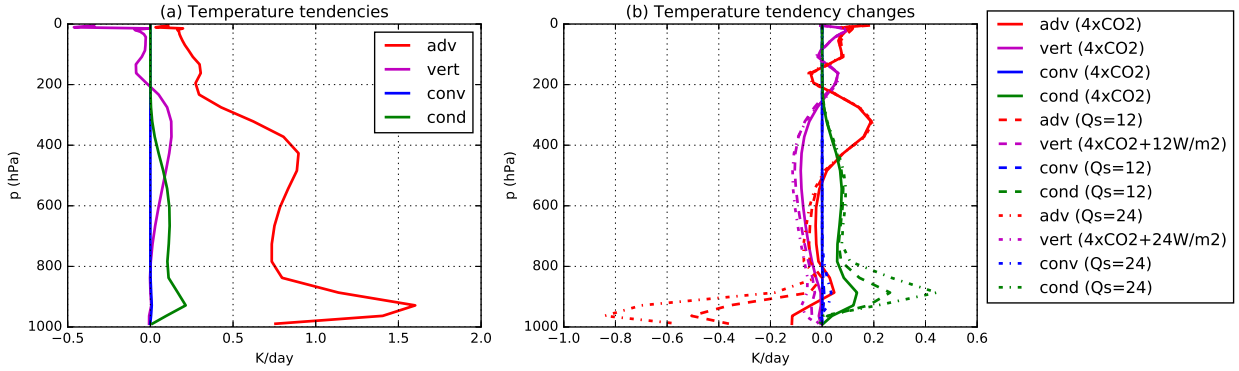

Fig. S2. (a) Climatological and (b) changes in idealized GCM temperature tendencies averaged poleward of 80° North. Shown are the dry ('adv' in red) and moist ('cond' in green) components of the energy transport, the vertical component of the advection term ('vert' in magenta), and the convective ('conv' in blue) temperature tendency. The first two are used as input to the single column model.

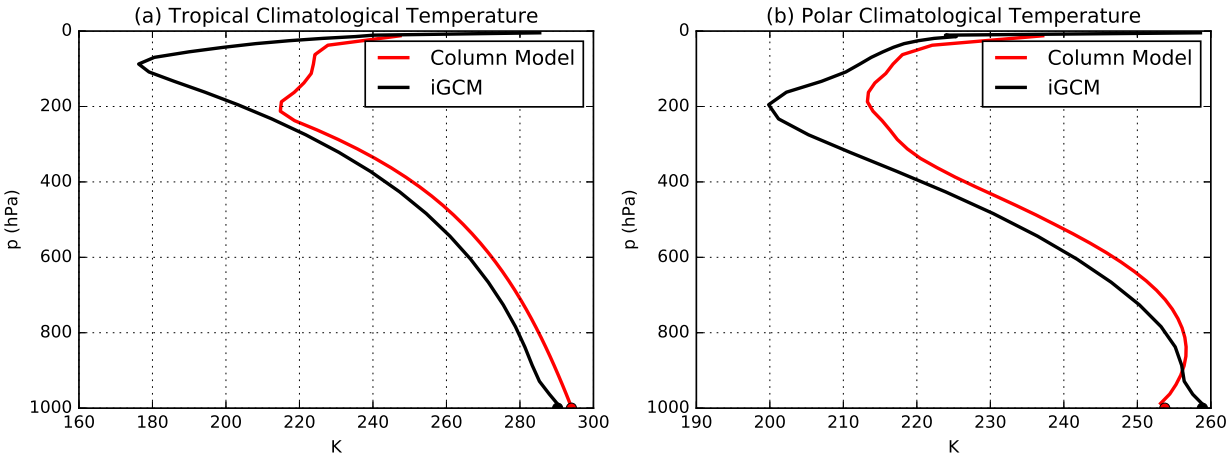

Fig. S3. Analog of figure 2 in the main text but with tropical and polar latitudinal bound set at 20° and 60° respectively. Climatological temperature of the idealized GCM (black) and the single column model (red).

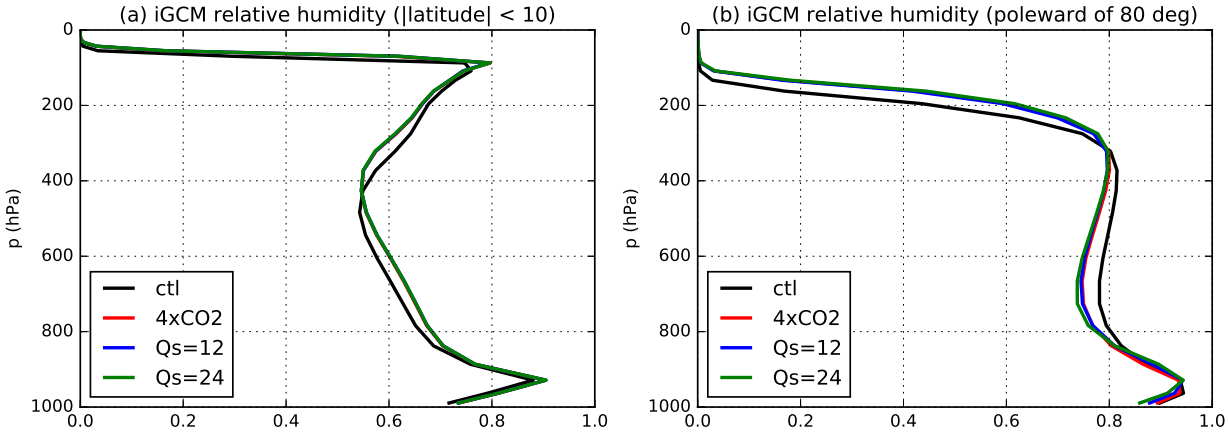

Fig. S4. Relative humidity of the idealized GCM averaged from -10° to 10° North (a) and poleward of 80° North (b) for the control (black), 4xCO_2 (red), 4xCO_2 with a 12 W m^{-2} surface heat source (blue), and 4xCO_2 with a 24 W m^{-2} surface heat source (green) simulations.

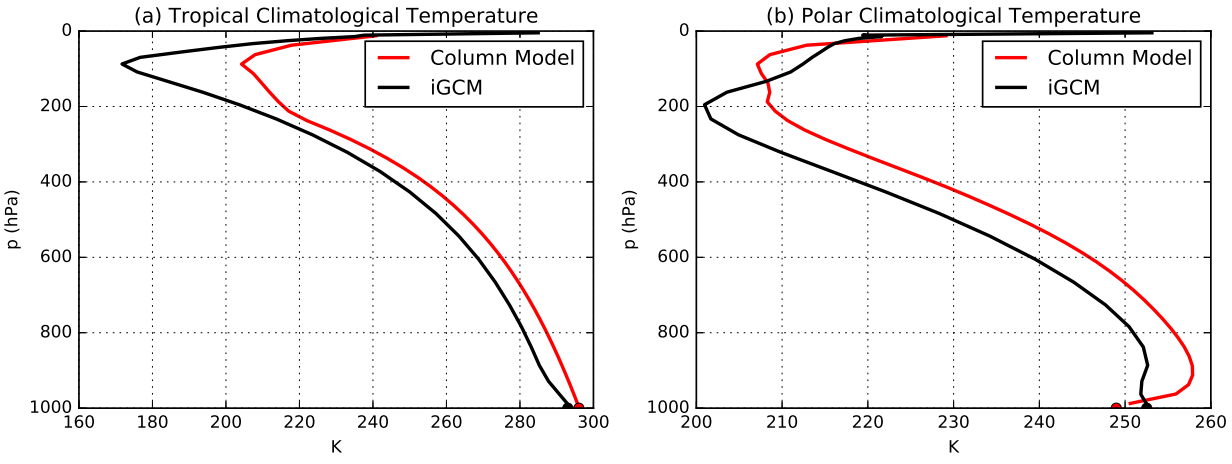

572 Fig. S5. Comparison of the climatological temperature of the fixed relative humidity single column model
573 (red) and the idealized atmospheric GCM (black) in the tropics (a) and the pole (b) for the 4xCO_2 experiment
574 only.

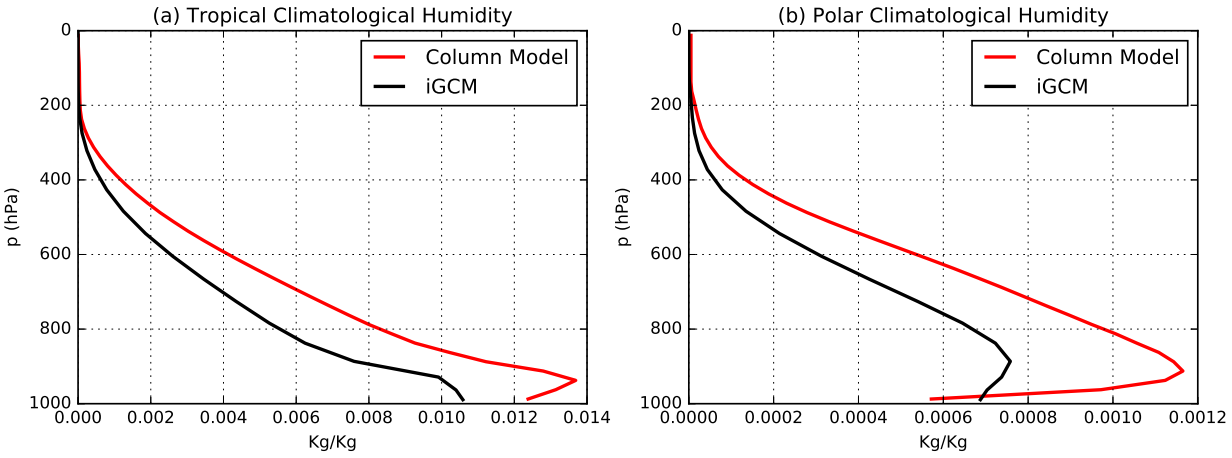

Fig. S6. Comparison of the climatological specific humidity of the fixed relative humidity single column model (red) and the idealized atmospheric GCM (black) in the tropics (a) and the pole (b) for the 4xCO_2 experiment only.

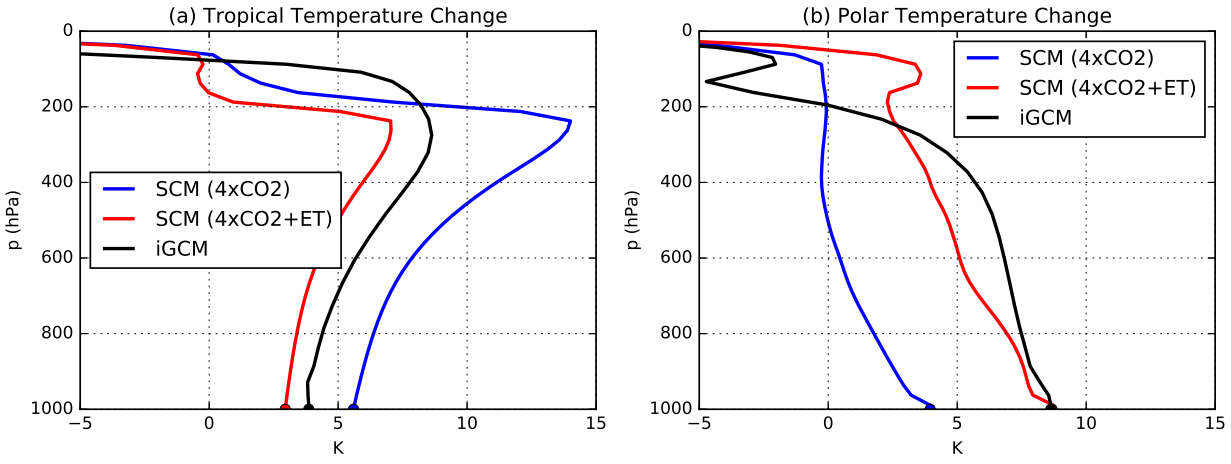

Fig. S7. Comparison of temperature change between the fixed relative humidity single column model (with control atmospheric energy transport (blue) and perturbed atmospheric energy transport (red)) and the idealized atmospheric GCM (black) in the tropics (a) and high latitudes (b) for the $4xCO_2$ experiment only.

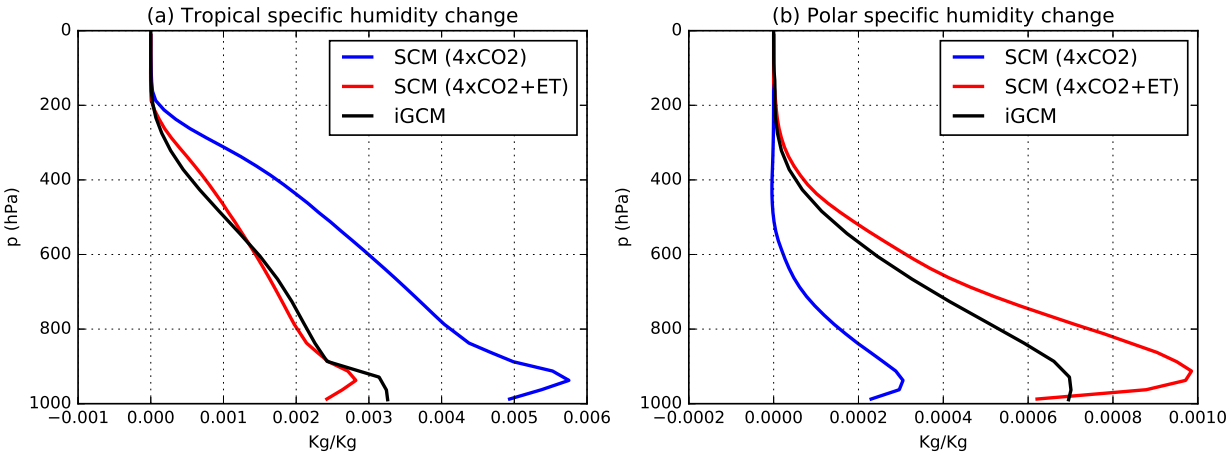

581 Fig. S8. Comparison of specific humidity change between the fixed relative humidity single column model
582 (with control atmospheric energy transport (blue) and perturbed atmospheric energy transport (red)) and the
583 idealized atmospheric GCM (black) in the tropics (a) and high latitudes (b) for the 4xCO_2 experiment only.